Check for updates

Relative water stability of powder *vs.* thin films of organic–inorganic halide perovskites including durability of a thin film bis(thiophenyl)-pyrrole lead iodide

Abdul Basit Naveed, [a] Matthew C. Mulvehill, [a] Aftab Javaid, [a] Craig A. Grapperhaus [b] and Joshua M. Spurgeon *[a]

Organic–inorganic halide perovskites are promising semiconductors for energy-conversion applications, but these materials face an inherent limitation due to poor intrinsic stability, particularly *via* decomposition upon exposure to water. The dimensionality and stability of perovskite materials are highly dependent on the organic cation in the perovskite. The incorporation of bulky organic ligands in the structure induces 2D layered perovskites where organic ligands are perpendicular to the inorganic layers and can enhance the perovskite moisture stability through the ligand hydrophobicity. Herein, the relative water stabilities of reportedly water-stable organic–inorganic halide perovskites were compared between microparticulate powders and compact thin films. In particular, the 3D perovskite $DMASnBr_3$ (DMA = dimethylammonium) and 2D perovskite $(PEA)_2SnBr_4$ (PEA = phenylethylammonium) were synthesized in both forms and characterized for water stability. The microparticulate crystals of both materials exhibited significant stability in water while analogous thin films were highly unstable, which was attributed to the presence of a soluble intermixed phase. A new bulky organic ligand, 8-(2,5-bis(thiophen-2-yl)-1*H*-pyrrol-1-yl)-octylammonium (2TPO), with hydrophobic wing-like groups to help impede water ingress was synthesized and incorporated into a 2D perovskite structure. A thin film of $(2TPO)_2PbI_4$ exhibited strongly enhanced durability when fully immersed in water for several minutes or exposed to 85% relative humidity for several days. Material stability was characterized using techniques such as X-ray diffraction (XRD), UV-visible spectroscopy, and X-ray photoelectron spectroscopy (XPS).

Introduction

Organic–inorganic hybrid perovskites have attracted tremendous attention because of their impressive semiconductor properties, rapid material development, and prospective low costs, leading to a prominent role as next-generation semiconductors for photovoltaic and optoelectronic applications.[1,2] The remarkable properties of organic–inorganic perovskites, including high optical absorption coefficients, relatively long minority-carrier diffusion lengths, effective charge transfer, and readily tunable band gaps by compositional variation, have made these materials very promising for solar energy conversion. Moreover, organometal halide perovskites can be synthesized from solution and coated on low-cost flexible substrates at low temperatures.[3] However, these materials face significant

stability challenges because moisture, heat, and UV light each can trigger the decomposition of the perovskite. To overcome water instability in particular, researchers have pursued various techniques including surface passivation and encapsulation to protect the perovskite from exposure. However, to make the photoactive material itself inherently resistant to moisture-induced breakdown, bulky hydrophobic organic ligands have been incorporated into the perovskite structure. These bulky organic ligands act as a hydrophobic barrier, thereby decreasing the interaction between water molecules and the underlying perovskite structure. The nature of the organic ligand must be considered for its effect on the perovskite optoelectronic properties as well, with long alkyl chain ligands typically increasing the band gap and resistance to charge transfer while conjugated ligands improve the charge transfer across the material and tend to decrease the band gap.[4]

Numerous combinations of organic–inorganic hybrid perovskites have been reported with the general chemical formula ABX_3. The BX_3 unit constructs an octahedron in which the B-site divalent metal cation occupies the center of the

[a] *Conn Center for Renewable Energy Research, University of Louisville, Louisville, Kentucky 40292, USA. E-mail: Joshua.spurgeon@louisville.edu*

[b] *Department of Chemistry, University of Louisville, 2320 South Brook Street, Louisville, Kentucky 40292, USA*

octahedron, and X-site halide anions reside at the corners. The octahedra are interconnected to each other to create a 3D perovskite framework, and these corner-sharing octahedra contribute to better charge transfer throughout the material by facilitating strong orbital overlap between neighboring atoms. The A-site cation is incorporated into the cavity created by eight interconnected octahedra, which is also referred to as a "perovskite cage". The size of the A-site cation can thus dictate the dimensionality of perovskite structures. Small A-site cations (*e.g.*, methylammonium) can be fully accommodated in the cavity of 3D perovskite structures. In contrast, if the A-site cation is bigger than the cavity of interconnected octahedra, it will break the 3D perovskite structure into a corresponding 2D perovskite.[5–7] Some 2D organic–inorganic hybrid perovskites anchored in a metal halide framework have exhibited promising optical properties while significantly enhancing the water stability relative to typical 3D organic–inorganic perovskites. The general chemical formula for quasi-2D perovskites is $(R–NH_3)_2A_{n-1}M_nX_{3n+1}$ where R is a bulky organic compound, A is a small organic cation, M is commonly Pb^{2+} or Sn^{2+}, and X is a halide anion.[8,9] The pure 2D perovskites are obtained at $n = 1$, when the steric hindrance of bulky organic ligands causes the separation of layers of inorganic metal halide octahedra. Generally, 2D perovskites build a layered structure by periodic splitting of 3D perovskites with a specific crystallographic plane, usually along the (100) plane.[10–14]

The moisture-induced breakdown of the organic–inorganic perovskite structure starts as water molecules adsorb on the material surface and initiate the formation of a monohydrate of the perovskite which further transforms into a dihydrate in high humidity or water immersion.[15] These hydrates are not stable and lead to degradation of the perovskite structure. Water molecules weaken the hydrogen bonding interaction between the organic cations and metal halide octahedra, resulting in rapid decomposition of the perovskite. Deprotonation of the organic cations by water further contributes to organometal halide perovskite breakdown.[16] The incorporation of largely nonpolar organic ligands imparts considerable hydrophobicity to the perovskite structure to limit the water degradation mechanism. Organic–inorganic perovskites incorporating dimethylammonium (DMA) cations, for instance, can accommodate the size of the DMA cation while retaining a 3D perovskite structure but are still reported to provide enhanced water stability. Microparticulates of $DMASnI_3$, $DMASnBr_3$, and $DMASnI_xBr_{3-x}$ have all exhibited material stability when immersed in liquid water for hours.[17–19]

Bulky organic ligands, in addition to imparting hydrophobic character, also can induce low dimensionality as described above. Both butylammonium (BA) and phenylethylammonium (PEA) have been reported as bulky organic ligands for hydrophobic 2D perovskites, which have been deposited as passivation layers on more traditional 3D perovskites to enhance the moisture stability of the composite material in humid environments.[20–22] The 2D perovskite $(PEA)_2SnBr_4$ has also been tested in microparticulate powder form, yielding stable material and optoelectronic properties after several hours of

water immersion.[23] However, due to insufficient hydrophobicity of the ligands, thin films of bithiophene and *n*-butylammonium-based 2D perovskites had poor stability in liquid water.[24] In contrast, tetrathiophene-based metal halide perovskite thin films were reported to exhibit stability for over a week in liquid water, indicating that well-designed organic ligands can significantly inhibit organic–inorganic perovskite decomposition even under full aqueous immersion. As another example, a thin film of (pyrene-*O*-propyl-NH$_3$)$_2$PbI$_4$ 2D perovskite showed material durability in liquid water for several minutes.[25]

Herein, representative cases of both 3D and 2D reportedly water-stable metal halide perovskite materials have been characterized in both powder and thin film form factors. Microparticulate crystalline powders of $DMASnBr_3$,[18] a 3D perovskite, and $(PEA)_2SnBr_4$,[23] a 2D perovskite, have both been reported with extended durability in water. Extrapolating these synthesis methods to equivalent thin film compositions, however, led to markedly different behavior and inferior durability, demonstrating the importance of the morphology and structure to the water stability. Moreover, a novel bulky organic ligand with two water-impeding hydrophobic thiophene wing-like groups, 8-(2,5-bis(thiophen-2-yl)-1*H*-pyrrol-1-yl)-octylammonium iodide (2TPOI), was synthesized to construct a new type of 2D perovskite capable of exhibiting strong water stability in thin film form as assessed by several complementary characterization techniques.

Experimental

Chemicals and materials

Hydrobromic acid (HBr, 48% in water), dimethylamine hydrochloride ($C_2H_7N·HCl$, 98%), tin(II) oxide (SnO, 99.99%), phenylethylammonium bromide (PEABr, 98%), tin(II) bromide ($SnBr_2$, 98%), hypophosphorous acid (H_3PO_2, 50% in water), dimethylammonium bromide (DMABr, 98%), dimethylformamide (DMF, 99.8%), lead(II) iodide (PbI_2, 99.99%), thiophene (C_4H_4S, 99%), succinyl chloride ((CH_2)$_2$(COCl)$_2$, 95%), dichloromethane (DCM, 99.9%), aluminum(III) chloride ($AlCl_3$, 99%), hydrochloric acid (HCl, 37% in water), 1,8-diaminooctane ($NH_2(CH_2)_8NH_2$, 98%), toluene ($C_6H_5CH_3$, 99.5%), titanium(IV) chloride ($TiCl_4$, 99.9%), methanol (CH_3OH, 99%), and hydroiodic acid (HI, 57% in water) were all purchased from Sigma Aldrich and used as received.

Synthesis of DMASnBr$_3$ and (PEA)$_2$SnBr$_4$ microparticulate powder

Both $DMASnBr_3$ and $(PEA)_2SnBr_4$ microparticulate powders were synthesized using a wet chemistry co-precipitation method. For $DMASnBr_3$, a solution was made by dissolving a mixture of SnO (6.0 mmol, 0.81 g) and $C_2H_7N·HCl$ (16.6 mmol, 1.35 g) into aqueous HBr (10 mL).[19] For $(PEA)_2SnBr_4$, a solution was made by dissolving PEABr (4.0 mmol, 0.808 g) and $SnBr_2$ (2.0 mmol, 0.56 g) into a mixture of aqueous HBr (3.0 mL) and H_3PO_2 (3.0 mL).[12] Each solution was heated at 100 °C under an
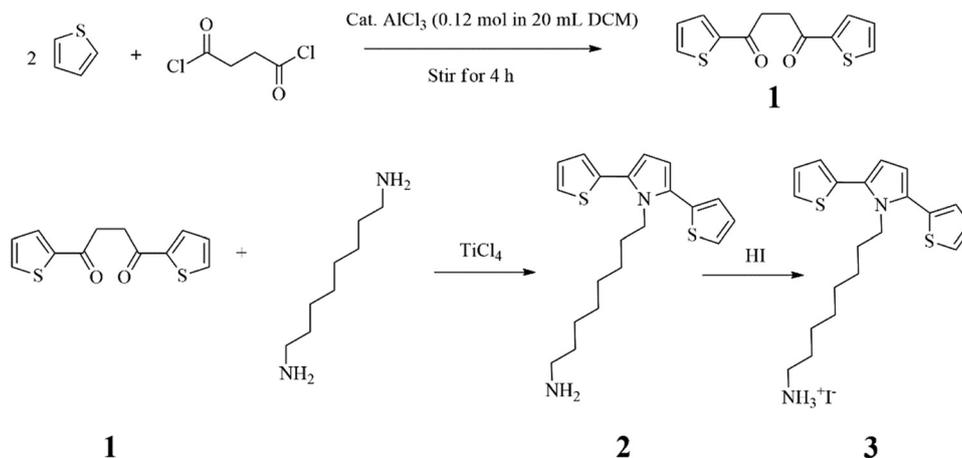
Scheme 1 Chemical synthesis pathway for the 2TPOI ligand (**3**).

inert Ar environment with constant stirring until the reactants were completely dissolved. Then, the solution was left at room temperature for the precipitation of the powder. The resulting yellow powders were washed with diethyl ether and dried using a rotatory evaporator.

Synthesis of DMASnBr$_3$, (PEA)$_2$SnBr$_4$ and (2TPO)$_2$PbI$_4$ thin films

Glass substrates were washed using acetone and isopropanol and treated with UV light for 10 min prior to perovskite material deposition. All thin film materials were prepared in a nitrogen-filled (<0.5 ppm O$_2$) glove box. To prepare the DMASnBr$_3$ thin film, DMABr (1.0 mmol, 0.126 g) and SnBr$_2$ (1.0 mmol, 0.278 g) were dissolved in 500 µL of anhydrous DMF. Then 100 µL of prepared solution was spin-coated on a glass substrate for 30 s at 2000 rpm, followed by annealing at 100 °C for 10 min to produce a $\sim$2 µm thick film. For (PEA)$_2$SnBr$_4$ thin films, PEABr (2.0 mmol, 0.404 g) and SnBr$_2$ (1.0 mmol, 0.278 g) were mixed in 500 µL of anhydrous DMF. Then 100 µL of the prepared solution was spin-coated onto a glass substrate for 30 s at 2000 rpm, followed by annealing at 130 °C for 10 min to produce a $\sim$1 µm thick film. For (2TPO)$_2$PbI$_4$ thin films, 2TPOI (200 µmol, 0.98 mg) and PbI$_2$ (100 µmol, 0.46 mg) were mixed in 250 µL of anhydrous DMF. Then, the prepared solution was spin-coated for 30 s at 2000 rpm, followed by annealing at 130 °C for 10 min to produce a $\sim$500 nm thick film.

Synthesis of 2TPOI

1,4-Bis(2-thiophen-2-yl)butane-1,4-dione[26] (1) (Scheme 1). Thiophene (0.12 mol, 10.0 g) and succinyl chloride (0.05 mol, 7.75 g) were mixed in 100 mL of DCM. A suspension of AlCl$_3$ (0.12 mol, 16.0 g) catalyst was made in 20 mL DCM in a two-necked round-bottom flask fitted with a stirrer, Ar inlet, and dropping funnel. The mixture of thiophene and succinyl chloride was added dropwise under Ar to the suspension of AlCl$_3$ over an ice bath. The resulting deep red solution was stirred for 4 h and subsequently changed into a red semisolid.

The semisolid product was dissolved in a stirred cold ($\sim$0 °C) dilute HCl solution (200 g ice melted in 5 mL conc. HCl) in an Erlenmeyer flask, and then 15 mL of DCM was added. A dark green organic layer was formed and then separated from the mixture using a separating funnel and sequentially washed with 2.0 M HCl followed by an aqueous 1.0 M NaHCO$_3$ solution to neutralize the acid. Finally, the solution was dried by adding anhydrous MgSO$_4$ which was subsequently filtered, and the solvent was then evaporated with a rotatory evaporator. When complete, a 50% yield for molecule (**1**) was obtained based on the mass. Molecule (**1**) was characterized by proton nuclear magnetic resonance (^{1}H-NMR) spectroscopy (Fig. S1), ^{13}C-NMR spectroscopy (Fig. S2), and Fourier transform infrared (FTIR) spectroscopy (Fig. S3).

8-(2,5-Bis(thiophen-2-yl)-1H-pyrrol-1-yl)-octylamine (2) (Scheme 1). 1,4-Bis(2-thiophen-2-yl)butane-1,4-dione (**1**) (4.0 mmol, 1.0 g) and 1,8-diaminooctane (19.4 mmol, 2.8 g) were mixed in 20 mL of toluene at 0 °C. After 30 min, TiCl$_4$ (4.0 mmol, 0.76 g) was dissolved into dry toluene and added dropwise to the reaction solution at 0 °C. The resulting solution was stirred for 1 h at room temperature and then slowly heated to 100 °C to reflux for 8 h. After that, the TiCl$_4$ salt was separated through filtration of the hot solution. The filtrate was washed with water three times to separate the unreacted diamine reactant from the product. Further, 8-(2,5-bis(thiophen-2-yl)-1H-pyrrol-1-yl)-octyl-amine (**2**) was extracted in toluene, and anhydrous MgSO$_4$ was added to the solution to absorb the water. The toluene was evaporated using a rotary evaporator, and the final product was obtained as a dark brown oil. Molecule (**2**) was characterized by ^{1}H-NMR spectroscopy (Fig. S4), ^{13}C-NMR spectroscopy (Fig. S5), and FTIR spectroscopy (Fig. S6).

8-(2,5-Bis(thiophen-2-yl)-1H-pyrrol-1-yl)-octylammonium iodide (2TPOI, 3) (Scheme 1). Compound (**2**) (1.3 mmol, 0.465 g), without any further purification, was dissolved in 15 mL of methanol and then HI (1.3 mmol, 0.17 mL) was added dropwise to the solution and stirred for 8 h at room temperature. The methanol was dried in a rotary evaporator, and the resulting mixture was washed with ether several

times. The final product was obtained as a yellow powder of ammonium salt. Molecule (**3**) was characterized by ^{1}H-NMR spectroscopy (Fig. S7), ^{13}C-NMR spectroscopy (Fig. S8), and FTIR spectroscopy (Fig. S9).

Materials characterization

Nuclear magnetic resonance (NMR) spectroscopy data was collected at room temperature using a Varian Inova 400 MHz NMR spectrometer. $CDCl_3$ and dimethylsulfoxide, DMSO-d_6 (Cambridge Isotopes, 99.9%), were used as solvents to prepare the samples for NMR characterization. To study the crystal structure, X-ray diffraction (XRD) analysis of powder and thin film samples was conducted using a Bruker D8 Discover X-ray diffractometer at room temperature using Cu Kα radiation (λ = 1.54056 Å). An Agilent 8453 diode array UV-Vis spectrophotometer was used to acquire the UV-visible (UV-Vis) absorbance data. Time-dependent UV-Vis data was collected using an Agilent Cary 60 spectrophotometer, where a thin film-coated glass substrate was placed inside a cuvette, and water was injected into the cuvette with a syringe during data collection. The contact angle for water on perovskite thin films was measured using an optical imaging goniometer (Biolin Scientific, Attension Theta Lite) in the static contact angle mode. For humidity exposure experiments, perovskite samples were kept in a chamber continuously purged with air of 85% relative humidity as monitored continuously by a relative humidity probe (Omega, RH-USB sensor). Humid air was generated by mixing controlled flow rates of dry air and air bubbled through a water reservoir. X-Ray photoelectron spectroscopy (XPS) with a VG Scientific Multilab 3000 custom-built ultrahigh vacuum (UHV) system with Al-Kα radiation was used to perform surface elemental analysis. A Thermo Fisher Nicolet iS20 FTIR spectroscope was used to record IR spectra. Electron micrographs of the morphology and elemental analysis of the organic–inorganic perovskite materials were performed with a Thermo Fisher Apreo C LoVac field emission scanning electron microscope (SEM) and energy-dispersive X-ray spectroscopy (EDS) detector.

Results and discussion

Microcrystalline powders of DMASnBr$_3$ and (PEA)$_2$SnBr$_4$

Both reportedly water-stable organic–inorganic perovskites, the 3D perovskite DMASnBr$_3$ and the 2D perovskite (PEA)$_2$SnBr$_4$, were synthesized in powder forms from literature methods. The synthesis of DMASnBr$_3$ was confirmed by matching the measured peak positions from XRD with the reported diffraction data.[17,18] The XRD peaks of 2D (PEA)$_2$SnBr$_4$ had periodic peaks at 10.7°, 16.2°, 21.9°, 27.2°, and 32.5°, in accordance with previous data which were assigned to the (002), (003), (004), (005), and (006) lattice planes, respectively.[12] EDS maps of both materials showed uniform distribution of the constituent elements (Fig. S10). The water stability of the microparticulates was assessed herein by XRD analysis before and after immersion of the powder in water and suspension of the particles under stirring for 2 h (Fig. 1). After the 2 h water exposure, the particles were allowed to settle, and the liquid water was separated by decanting. XRD was separately conducted on both the settled powder (*i.e.*, the precipitate) and the residue left behind after drying the decanted liquid water (*i.e.*, the supernatant). In addition to the XRD, Fig. 1 shows optical images of the yellow perovskite powders as prepared and as recovered from the water-immersed precipitate.

In the case of both DMASnBr$_3$ and (PEA)$_2$SnBr$_4$, the bulk of the powder was water stable and recovered from the precipitate after stirring. Macroscopically, the powder color and grain morphology were essentially unchanged. SEM characterization showed bulk microparticulate crystals of the DMASnBr$_3$ powder and a flakier morphology for the (PEA)$_2$SnBr$_4$ consistent with its
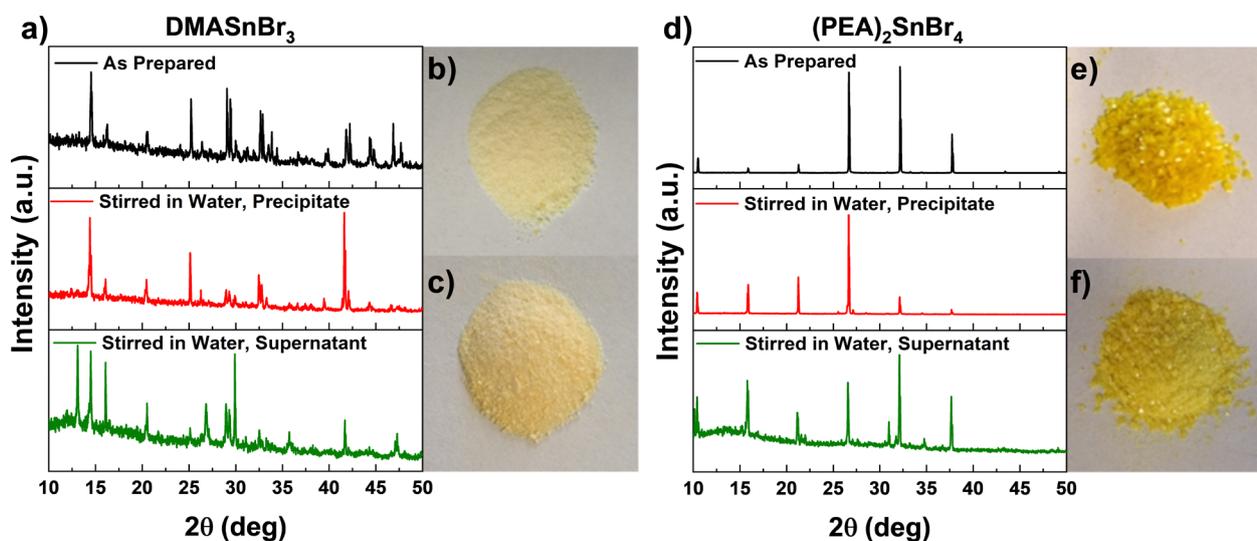

Fig. 1 Water stability of microcrystalline powder forms of (a)–(c) DMASnBr$_3$ and (d)–(f) (PEA)$_2$SnBr$_4$ perovskites. (a) and (d) XRD data for the powders as prepared (black) and after 2 h of stirring in water then settling and decanting, with analysis of the precipitate (red) and the dried supernatant (green). Photographs are also shown of the powders (b) and (e) as prepared and (c) and (f) as precipitate after 2 h stirred in water.
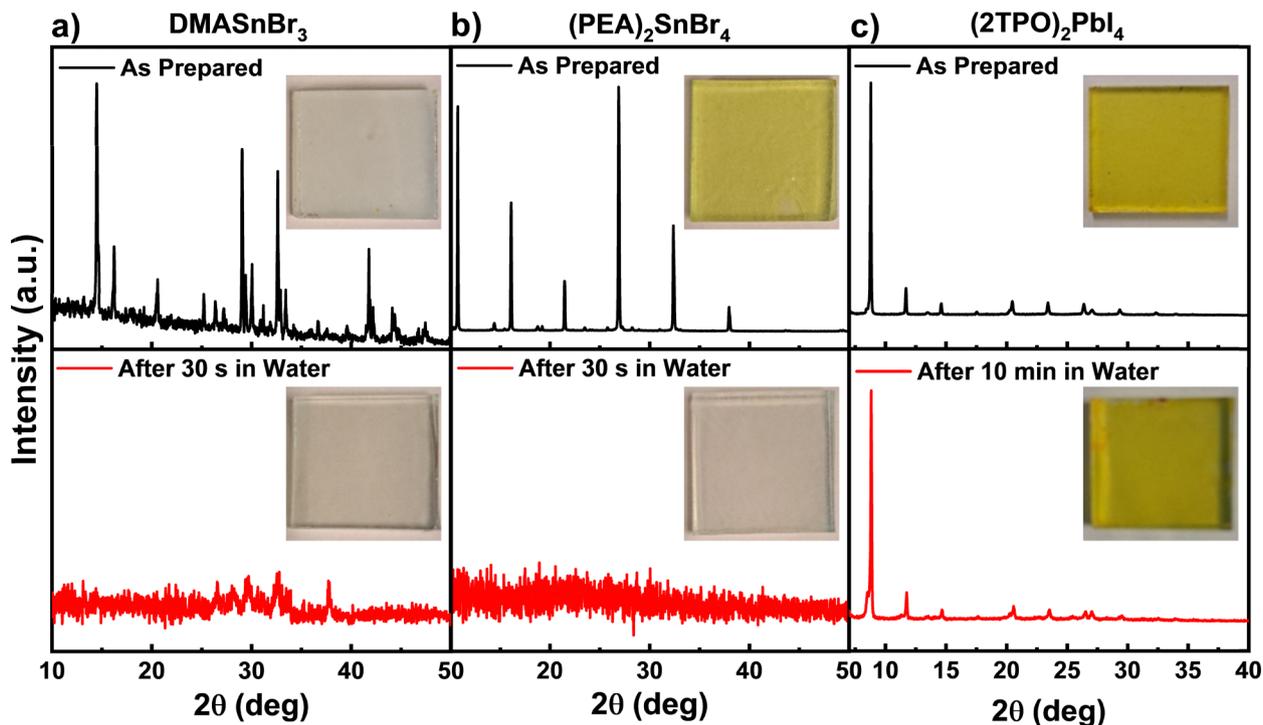
Fig. 2 Water stability of thin film forms of (a) DMASnBr$_3$, (b) (PEA)$_2$SnBr$_4$, and (c) (2TPO)$_2$PbI$_4$ perovskites. (a)–(c) XRD data for the thin films as prepared (black) and after immersion in water (red) for either 30 s or 10 min. Insets show corresponding photographs of the thin film samples on a glass substrate.

2D structure, and neither exhibited obvious morphological changes after water exposure (Fig. S11). However, for both perovskites the diffractogram of the post-immersion precipitate exhibited changes from the as-prepared material. Although many of the peaks observed for as-prepared DMASnBr$_3$ were present at similar intensities in the precipitate (*e.g.* 14.5°, 16.0°, 20.6°, 25.2°), some others were significantly decreased in intensity (*e.g.*, 29.3°, 44.4°, 46.9°), and the peak at 41.7° sharply increased (Fig. 1(a)). In contrast, the residue from the DMASnBr$_3$ supernatant exhibited some peaks that were far more intense than in the precipitate (*e.g.*, 13.1°, 16.0°, 29.9°, 35.9°, 47.0°). Similarly, the diffractogram of the (PEA)$_2$SnBr$_4$ precipitate had a few strongly decreased peak intensities (*e.g.*, 32.5°, 37.7°) and other increased peak intensities (*e.g.*, 16.2°, 21.9°) relative to the as-prepared material (Fig. 1(d)). For (PEA)$_2$SnBr$_4$, the residue from the supernatant exhibited the same peak positions as the as-prepared material with a much sharper peak at 37.7° than exhibited by the precipitate, indicating that this peak may be attributable to a water-soluble phase. Additionally for the supernatant residue from (PEA)$_2$SnBr$_4$, new peaks appeared at 30.9° and 34.7°, which may be indicative of water-induced decomposition products. Thus, although the bulk of both DMASnBr$_3$ and (PEA)$_2$SnBr$_4$ perovskite powders displayed strong water stability for the material composition and crystallinity, the XRD results are consistent with the as-prepared powders containing domains of water-unstable phases.

Thin films of DMASnBr$_3$ and (PEA)$_2$SnBr$_4$

For applications such as intrinsically water-tolerant photovoltaics or certain reactor designs for photoelectrochemical

water-splitting, a contiguous thin film perovskite form factor would be more amenable than microparticulates to a high-performance device. Thus, the solution-based syntheses of DMASnBr$_3$ and (PEA)$_2$SnBr$_4$ were modified to a spin-coating method to produce uniform thin film deposits on glass. XRD diffractograms for as-prepared DMASnBr$_3$ (Fig. 2(a)) and (PEA)$_2$SnBr$_4$ (Fig. 2(b)) displayed the same set of peak positions and relative intensities that were exhibited in the XRD for powder samples (Fig. 1), indicating retention of the corresponding perovskite structure in the thin film. While the (PEA)$_2$SnBr$_4$ film was a vibrant yellow color, the DMASnBr$_3$ film was a dull cloudy bluish color. Unlike the analogous powder samples, both thin film materials rapidly degraded within seconds by visual observation when immersed in liquid water. Indeed, XRD characterization of the samples after only 30 s of water exposure yielded an absence of discernible peaks (Fig. 2(a) and (b)), indicating complete removal of the film from the glass substrate. Gravimetric measurements of the glass substrate also failed to detect any perovskite mass remaining after the water immersion period.

The drastic decline in the apparent water stability of the thin film organic–inorganic perovskites, despite the relative stability of the bulk of powders of the same composition and crystallinity, suggests that morphology played a critical role in the water-induced degradation. Notably, the perovskite thin film diffractograms contained the same peaks that were present in the as-prepared microparticulate powders but were mostly removed in the stable precipitate (*e.g.*, 29.3°, 46.9° for DMASnBr$_3$ and 32.5°, 37.7° for (PEA)$_2$SnBr$_4$). Thus, the instability of the

thin films is consistent with the presence of an intermixed phase of soluble material, which upon dissolution results in the collapse of the contiguous film morphology and delamination from the substrate.

Thin films of $(2TPO)_2PbI_4$

Because $DMASnBr_3$ and $(PEA)_2SnBr_4$ could not readily have their powder form water stability extended to a thin film morphology, the need remains for a promising organometal halide perovskite with water stability when directly cast in thin film form. Although the stabilized precipitate phase of the $DMASnBr_3$ and $(PEA)_2SnBr_4$ powders could presumably be recast as a stable microparticulate film on a substrate, the resulting layer would suffer from pinholes, grain boundaries, and limited cross-particle conductivity. Instead, a new bulky organic ligand for incorporation into a 2D perovskite structure was tested for water stability in a compact thin film layer.

The bulky organic ligand 8-(2,5-bis(thiophen-2-yl)-1H-pyrrol-1-yl)-octylammonium iodide (2TPOI) (Scheme 1) was synthesized with the aim of making a strongly hydrophobic organic group that could be accommodated in a 2D metal halide perovskite. The octane chain was attached to increase the solubility of the ligand in nonpolar solvents to prepare the homogeneous solution of perovskite for coating a uniform thin film. Moreover, the hydrophobicity of the long alkane chains should protect the perovskite structure from moisture and reduce the π–π stacking interactions among the organic ligands, which cause aggregation and detrimentally affect the material performance. The eight-carbon chain also serves as a spacer to decrease steric hindrance between the adjacent bulky conjugated bis(thiophenyl)-pyrrole groups while enabling the accessibility of hydrogen bonding between the ammonium cation and the inorganic lead iodide octahedra. Moreover, it was hypothesized that the two hydrophobic thiophene wings protruding from the ligand's pyrrole end group may partially overlap between adjacent ligands and enhance water stability by providing an umbrella-like barrier layer to further prevent the ingress of water molecules to the inorganic layer. A schematic of the novel $(2TPO)_2PbI_4$ 2D perovskite structure is shown in Fig. 3(a).

To verify formation of the 2D perovskite structure, the $(2TPO)_2PbI_4$ thin film was characterized and compared to the individual component reactants used in its synthesis, the organic ligand ammonium salt, 2TPOI, and lead iodide, PbI_2. Fig. 3(b) shows the XRD data, in which the distinctive peaks of the organic cation salt 2TPOI appeared at 7.4° and 14.6°, and PbI_2 exhibited prominent peaks at 12.6° and 38.5°. When reacted and cast as a thin film, the appearance of new peaks and the absence of the characteristic peaks of the reactants in the XRD pattern indicated the formation of a new crystal structure corresponding to a 2D perovskite.[27] For $(2TPO)_2PbI_4$, XRD peaks appeared at 8.7°, 11.7°, 14.6°, 17.5°, 20.5°, 23.4°, and 26.4°.

Similarly, the UV-vis absorbance spectra for $(2TPO)_2PbI_4$ thin films was distinct from either the organic ligand salt or PbI_2, indicating the formation of a new perovskite with higher
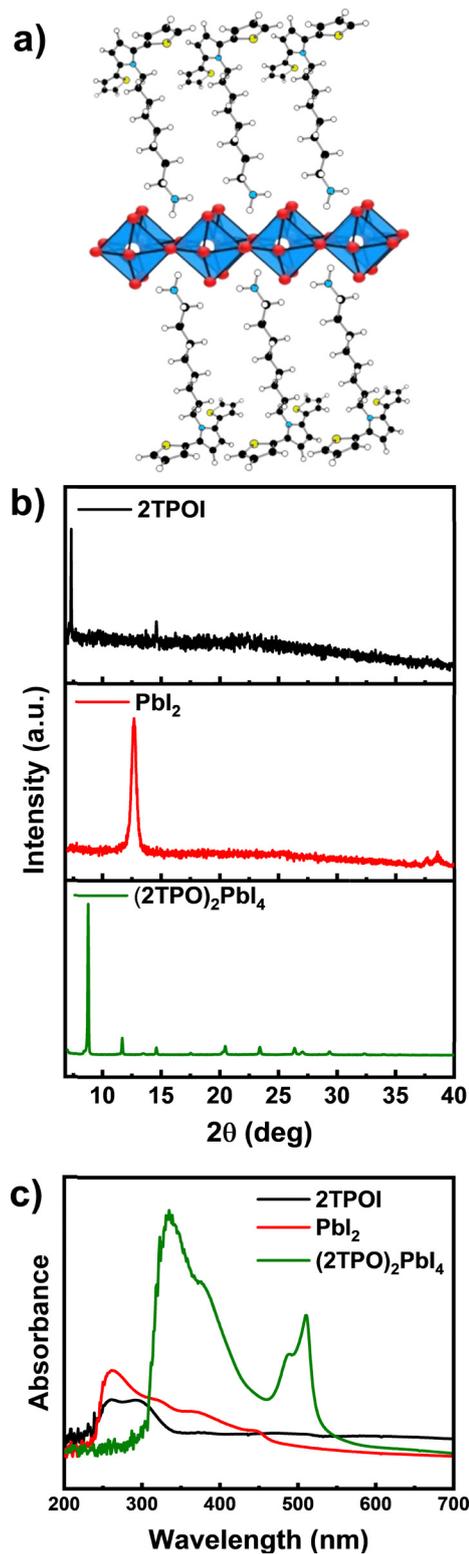

Fig. 3 (a) Schematic of the perovskite structure with 2TPO ligands coordinated with lead iodide octahedra. (b) XRD data and (c) UV-Vis absorbance spectra for $(2TPO)_2PbI_4$ thin film and both of its precursor compounds, showing the distinct behavior of the new perovskite composition.

absorption in the visible spectrum (Fig. 3(c)).[28,29] 2D perovskites commonly show two different absorbance peaks in the
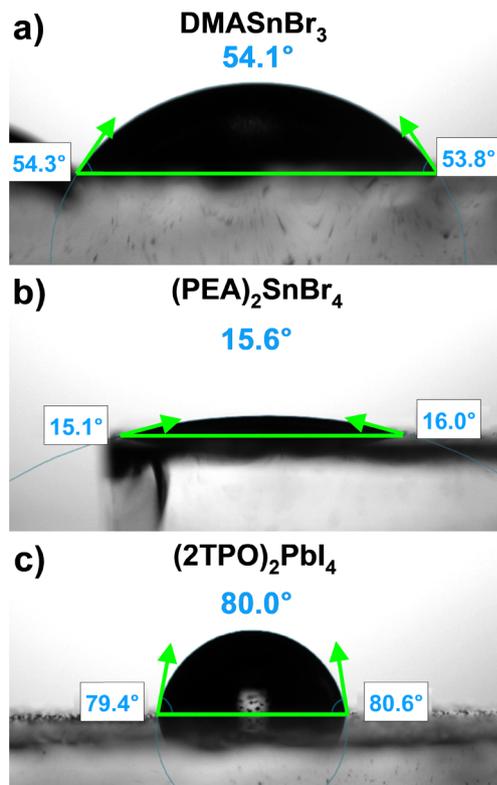
Fig. 4 Contact angle measurements for water droplets on thin films of (a) DMASnBr₃, (b) (PEA)₂SnBr₄, and (c) (2TPO)₂PbI₄. The angle shown above the droplet is the average of measurements from both sides of the droplet image.

UV-visible spectrum which have been attributed to the alternating organic and inorganic layers.[24,30,31] The inorganic units act as quantum wells which absorb at longer wavelengths, and the organic layers act as wide bandgap insulating barriers that result in absorption at shorter wavelengths.[32] The inorganic unit of $(2TPO)_2PbI_4$ exhibited an absorption peak at 503 nm, and the organic layer showed absorption in the UV region peaking at 330 nm attributable to high energy transitions ($\sigma-\sigma^\star$ and $\pi-\pi^\star$) of the aliphatic and aromatic groups.

The novel 2D perovskite $(2TPO)_2PbI_4$ was cast as a thin film and investigated for intrinsic water stability. The sample made a bright yellow film on the glass substrate, and unlike $(PEA)_2SnBr_4$, the yellow film was retained even after 10 min of full immersion in liquid water (Fig. 2(c)). Moreover, the diffractogram of the film after water immersion preserved the positions and relative intensities of the peaks measured for the as-prepared material without any distinct new peaks that might indicate phase segregation or decomposition. The post-immersion diffractogram did however exhibit a slight broadening of the peak at 8.7°, which was attributed to the penetration of water molecules into the perovskite crystal in the outer layers of the $(2TPO)_2PbI_4$ thin film consistent with the early stages of metal halide perovskite hydration.[15] Thus, the structure and hydrophobic nature of the 2TPO ligand, along with the ability to deposit the perovskite in a contiguous single-phase crystalline thin film, led to a major enhancement in the water stability of the $(2TPO)_2PbI_4$ compared to the thin films of DMASnBr₃ and $(PEA)_2SnBr_4$ (Fig. 2). For comparison, while most literature reports analyzing metal halide perovskite stability

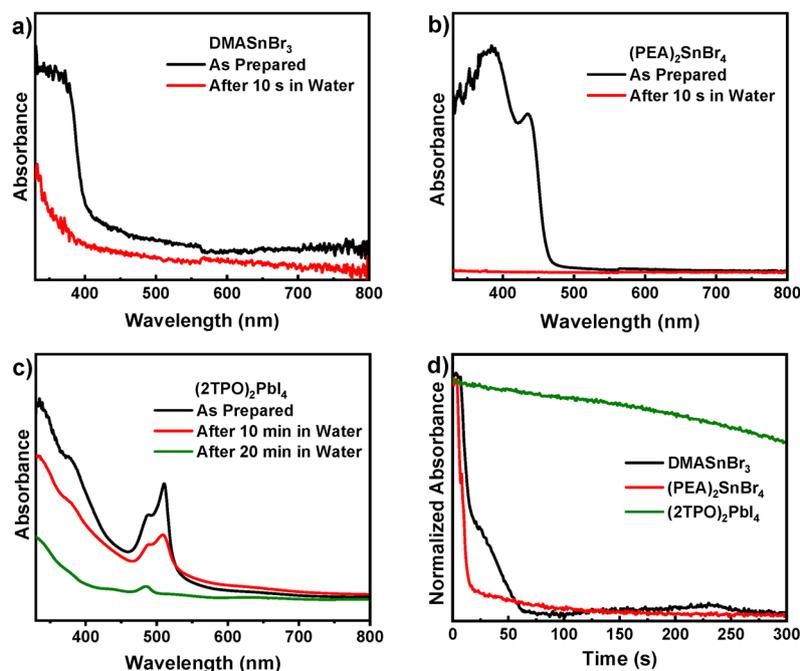Fig. 5 Water immersion effects on the (a)–(c) optical absorbance measured by UV-Vis of thin film forms of (a) DMASnBr₃, (b) (PEA)₂SnBr₄, and (c) (2TPO)₂PbI₄ perovskites. (d) Time-dependent normalized absorbance of perovskite thin films with liquid water added to the cuvette at time = 0 s. Each time-dependent curve was measured at a wavelength of strong absorbance for that material (390 nm for DMASnBr₃, 440 nm for (PEA)₂SnBr₄, and 510 nm for (2TPO)₂PbI₄).

immersed in liquid water have relied on powder forms,[33] a thin film of a quasi-2D carbazole (CA) methyl ammonium (MA) lead iodide, $CA_2MA_4Pb_5I_{16}$, has been reportedly stable for direct water immersion for more than 5 min.[34]

The relative hydrophobicity imparted to the perovskite *via* the 2TPO organic ligands was highlighted by contact angle measurements of water droplets on the thin films (Fig. 4). The average contact angle was 54.1° and 15.6° for $DMASnBr_3$ and $(PEA)_2SnBr_4$, respectively. The low contact angle for $(PEA)_2SnBr_4$ is consistent with a reported low contact angle for quasi-2D perovskite thin films with PEA cations at the surface.[34] In contrast, the contact angle increased to 80.0° for the $(2TPO)_2PbI_4$ thin film, highlighting the improved hydrophobicity of the ligand and its role in promoting greater durability of the material in water *via* hydrophobic shielding.

The effect of water on the optical absorption properties of $DMASnBr_3$, $(PEA)_2SnBr_4$, and $(2TPO)_2PbI_4$ thin films was also investigated *via* UV-Vis spectroscopy (Fig. 5). Prior to water immersion, the $DMASnBr_3$ absorbance peaked at a high energy photon wavelength of 390 nm. $(PEA)_2SnBr_4$ is also a wide bandgap material and exhibited strong absorbance at 440 nm. The $(2TPO)_2PbI_4$ thin film had an absorption band edge at lower wavelengths, with an absorbance peak at 503 nm. The narrower bandgap for $(2TPO)_2PbI_4$ is attributable to the lower electronegativity of iodine relative to bromine as the perovskite halide. Stronger ionic interactions due to high electronegativity can lower the energy of the valence band edge and widen the bandgap.[35]

Within 10 s immersed in water, $DMASnBr_3$ and $(PEA)_2SnBr_4$ thin films both exhibited a near total decrease in absorbance (Fig. 5(a) and (b)), consistent with the rapid water-induced degradation described above. The $(2TPO)_2PbI_4$ perovskite thin film displayed the same absorption pattern after a 10 min immersion in water with only a modest decrease in the absorbance magnitude, indicating that the bulkier hydrophobic ligand with the bis(thiophenyl)-pyrrole head group strongly impeded the water-induced degradation process. Still, further immersion of the film in water led to the gradual decline of the peak at 503 nm, as evidenced by the UV-Vis spectra after 20 min in water (Fig. 5(c)). The decrease in this absorbance peak reflects the slow decomposition of the inorganic units consistent with the greater reactivity of PbI_4^{2-} with water than its organic counterpart. The improved water stability of $(2TPO)_2PbI_4$ relative to the other thin films is further conveyed by observing the transient UV-Vis data for each film at a wavelength near its maximum absorbance when first exposed to water (Fig. 5(d)). The data is plotted as the absorbance normalized to its initial value. For each sample, the cuvette was filled with water in the first 5 s, and subsequently a rapid decline in absorbance was observed for $DMASnBr_3$ and $(PEA)_2SnBr_4$. In contrast, the $(2TPO)_2PbI_4$ thin film was more durable in liquid water, with the absorbance dropping 25% after 5 min. Thus, while the hydrophobic ligand and single-phase thin film deposition enhanced the $(2TPO)_2PbI_4$ perovskite durability, further improvements are still needed for sufficiently intrinsic water stability for prolonged aqueous operation.

Although conditions of liquid water immersion are of interest for potential applications of metal halide perovskites in photocatalytic and solar water-splitting devices,[33] for strictly photovoltaic applications the exposure of thin films to liquid water represents an accelerated stress test for degradation *via* hydration.[15] For photovoltaics, moisture stability is more commonly investigated by prolonged exposure to high humidity conditions. Thus, thin films of $(2TPO)_2PbI_4$ were further characterized by regular UV-Vis spectroscopic measurements over six days of exposure to air maintained at 85% relative humidity (Fig. 6). Over this time, the absorbance at ∼503 nm, which was correlated to the inorganic unit of the perovskite, slowly but steadily declined and lost 24% of the peak absorbance by day 6. The moisture stability of the film can be considered relative to the many reports of metal halide perovskite solar cells under humidity.[36] Notably, however, the $(2TPO)_2PbI_4$ layer was directly exposed to moist air without the benefit of slowed water ingress due to a surface coating of an electron or hole transport layer or top-contact layer that would be present in full photovoltaic devices. The absorbance peak position also underwent a slight
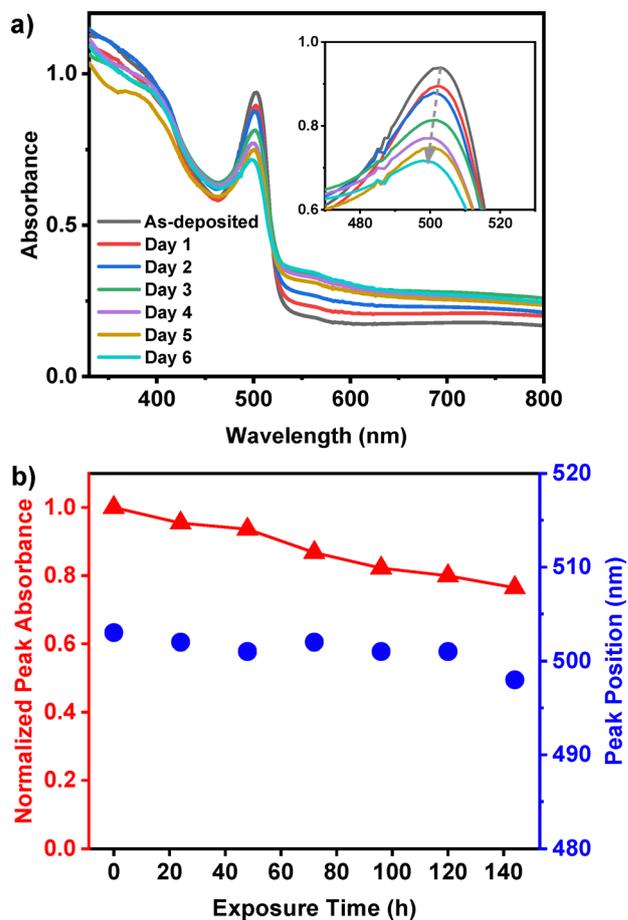

Fig. 6 (a) UV-Vis absorbance spectra for the $(2TPO)_2PbI_4$ thin film during continuous exposure to air of 85% relative humidity at room temperature, with an inset showing a zoomed-in view of the absorbance peak. (b) The absorbance peak normalized to the peak value for the as-deposited film (left axis, red) and the wavelength peak position (right axis, blue) *vs.* exposure time to 85% relative humidity.

spectral shift from 503 to 498 nm over this duration. The gradual absorbance decline is consistent with known mechanisms of metal halide perovskite hydration under high humidity in which the infiltration of water molecules into the lattice and subsequent hydrogen bonding leads to the formation of mono- and dihydrate perovskites which impede the optoelectronic activity.[15]

Further materials characterization of the thin film $(2TPO)_2PbI_4$ perovskite provided insight on the nature of the water-induced degradation process. SEM imaging of the thin film surface before and after 10 min in liquid water indicated only minor morphological changes occurred (Fig. 7(a) and (b)). As prepared, the perovskite film was fairly smooth at the micron scale, and it mostly remained so after water immersion, with only a few observable depressions that may indicate the start of corrosive pitting. Additionally, XPS characterization probed the surface chemical state of the $(2TPO)_2PbI_4$ before and after water immersion (Fig. 7(c) and (d)). The slight decrease in peak intensity after 10 min in water could be attributable to pinhole formation reducing the perovskite sampling area. However, the peak positions for both the I 3d and Pb 4f binding energies remained nearly constant after water immersion, indicating no change in the chemical state of the perovskite surface. Individual XPS spectra with peak fitting are shown in Fig. S12 with quantitative data given in Table S1. The I $3d_{5/2}$ and Pb $4f_{7/2}$ peaks for $(2TPO)_2PbI_4$ were measured at 618.8 eV and 138.2 eV, respectively, which is almost identical to the reported binding energies of the corresponding orbitals in other organometal halide perovskites like $CH_3NH_3PbI_3$.[37] Organic lead halide perovskites commonly decompose into phases including metallic Pb^0 and PbI_2, which can then be

oxidized to form PbO when exposed to air. Metallic lead has a binding energy of 136.8 eV, and a surface PbO leads to a broadening of the peak. Similarly, organic lead iodide perovskite decomposition reportedly shifts the I $3d_{5/2}$ peak from 618.8 eV toward 619.5 eV.[37] This type of XPS peak broadening and shifting was not observed in the post-water-immersion spectra of $(2TPO)_2PbI_4$, indicating that the chemical environment of the surface elements in the perovskite material were unchanged after 10 min in water. The slow water degradation process of $(2TPO)_2PbI_4$ is thus assumed to proceed through gradual dissolution with little to no residual chemical decomposition products left at the surface.

Conclusions

Developing intrinsically water-stable organic–inorganic halide perovskites would allow for long-term durability in photovoltaic applications and enable their use in photoelectrochemical water-splitting. Two reported water-stable organometal halide perovskites, $DMASnBr_3$ and $(PEA)_2SnBr_4$, were studied as powders and thin films to investigate their relative stability in morphologies amenable to device fabrication. Although crystalline powders showed stability of the bulk of the particulates in water, XRD of the residue from the supernatant indicated that a portion of the mixed-phase material was susceptible to dissolution. Thus, when translated to a thin film morphology, both organic–inorganic halide perovskites rapidly degraded due to delamination and dissolution of the insufficiently hydrophobic mixed phase. The design of a novel organic ligand functionalized
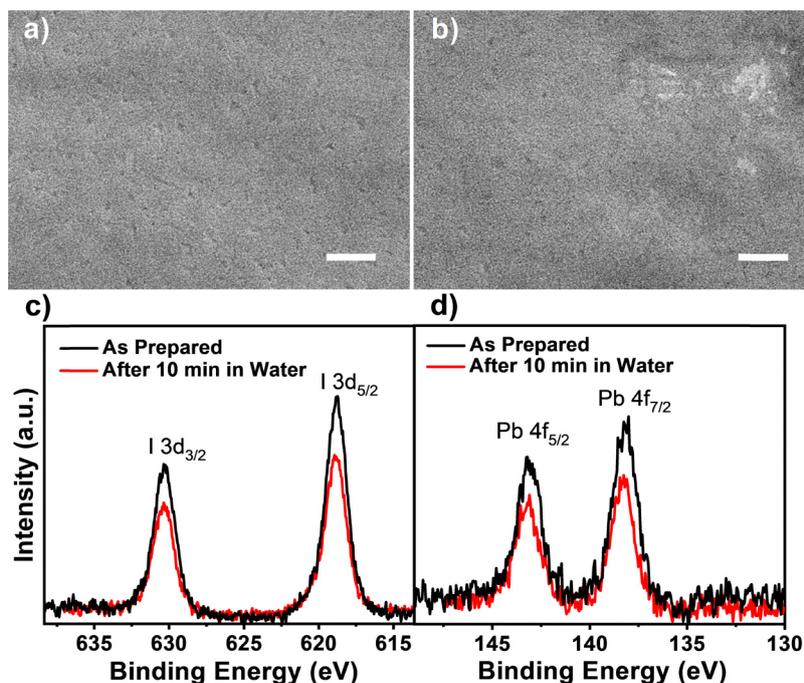

Fig. 7   SEM images of a $(2TPO)_2PbI_4$ thin film (a) before and (b) after 10 min immersed in water. The scale bar is 1 μm in both. XPS spectra of the (c) I 3d and (d) Pb 4f regions for thin films of $(2TPO)_2PbI_4$ perovskite before (black) and after 10 min immersed in water (red).

with thiophenyl wing groups on a pyrrole head group separated from the metal halide octahedra by a hydrophobic alkyl chain led to the synthesis of a single-phase low-dimensional perovskite that enhanced the resistance of the thin film against water-induced degradation. The $(2TPO)_2PbI_4$ thin film retained its crystalline structure when immersed in liquid water for $>60\times$ the duration that led to full removal of $DMASnBr_3$ and $(PEA)_2SnBr_4$ thin films. Although UV-Vis data indicated gradual dissolution of the $(2TPO)_2PbI_4$, XPS spectra demonstrated a stable chemical state of the metal halide surface components.

The 2TPO ligand, as a bulky hydrophobic organic group with steric hindrance from the bis(thiophenyl)-pyrrole, breaks up the lead iodide layering to form a 2D perovskite. A $(2TPO)_2PbI_4$ 2D perovskite layer would therefore be a strong candidate for surface passivation of more efficient photoactive 3D organic–inorganic halides for the water stabilization of perovskite solar cells. Use of the 2D perovskite semiconductor in applications for solar water-splitting would require advances in the ligand structure to further amplify the intrinsic water stability and possibly extended conjugation to improve charge-carrier mobility throughout the film.

Author contributions

The project was conceived by J. M. S. and C. A. G. and carried out under their guidance and mentorship. A. B. N. conducted the majority of the experiments, including perovskite synthesis and materials characterization. M. C. M. performed SEM and EDS characterization. A. J. aided with material characterization and manuscript preparation. C. A. G. oversaw organic ligand and perovskite synthesis. J. M. S. oversaw material testing, characterization, and interpretation. A. B. N. and J. M. S. wrote the manuscript, and all authors contributed to editing it.

Conflicts of interest

There are no conflicts to declare.

Data availability

The data supporting this article have been included as part of the supplementary information (SI). The supplementary information contains NMR and FTIR spectra relevant to the synthesis of 2TPOI, SEM and EDS of microparticulate powders, and XPS surface analysis of $(2TPO)_2PbI_4$ thin films. See DOI: https://doi.org/10.1039/d5ma00617a.

Acknowledgements

Notes and references

1 Y. Zhao and K. Zhu, *Chem. Soc. Rev.*, 2016, **45**, 655–689.
2 K. Zhou, B. Qi, Z. Liu, X. Wang, Y. Sun and L. Zhang, *Adv. Funct. Mater.*, 2024, **34**, 2411671.
3 S. Sun, M. Liu, J. Thapa, N. T. P. Hartono, Y. Zhao, D. He, S. Wieghold, M. Chua, Y. Wu, V. Bulovic, S. Ling, C. J. Brabec, A. I. Cooper and T. Buonassisi, *Chem. Mater.*, 2022, **34**, 9384–9391.
4 H. Zubair, R. F. Mahmood, M. Waqas, M. Ishtiaq, J. Iqbal, M. A. A. Ibrahim, S. R. M. Sayed, S. Noor and R. A. Khera, *RSC Adv.*, 2023, **13**, 26050–26068.
5 Y. Fu, X. Jiang, X. Li, B. Traore, I. Spanopoulos, C. Katan, J. Even, M. G. Kanatzidis and E. Harel, *J. Am. Chem. Soc.*, 2020, **142**, 4008–4021.
6 X. Li, S. A. Cuthriell, A. Bergonzoni, H. Dong, B. Traore, C. C. Stoumpos, P. Guo, J. Even, C. Katan, R. D. Schaller and M. G. Kanatzidis, *Chem. Mater.*, 2022, **34**, 1132–1142.
7 X. Li, H. Dong, G. Volonakis, C. C. Stoumpos, J. Even, C. Katan, P. Guo and M. G. Kanatzidis, *Chem. Mater.*, 2022, **34**, 6541–6552.
8 L. Mao, C. C. Stoumpos and M. G. Kanatzidis, *J. Am. Chem. Soc.*, 2019, **141**, 1171–1190.
9 L. Mao, W. Ke, L. Pedesseau, Y. Wu, C. Katan, J. Even, M. R. Wasielewski, C. C. Stoumpos and M. G. Kanatzidis, *J. Am. Chem. Soc.*, 2018, **140**, 3775–3783.
10 J. Hu, L. Yan and W. You, *Adv. Mater.*, 2018, **30**, 1802041.
11 X. Li, J. M. Hoffman and M. G. Kanatzidis, *Chem. Rev.*, 2021, **121**, 2230–2291.
12 L.-J. Xu, H. Lin, S. Lee, C. Zhou, M. Worku, M. Chaaban, Q. He, A. Plaviak, X. Lin, B. Chen, M.-H. Du and B. Ma, *Chem. Mater.*, 2020, **32**, 4692–4698.
13 L. Lanzetta, J. M. Marin-Beloqui, I. Sanchez-Molina, D. Ding and S. A. Haque, *ACS Energy Lett.*, 2017, **2**, 1662–1668.
14 E. Amerling, S. Baniya, E. Lafalce, C. Zhang, Z. V. Vardeny and L. Whittaker-Brooks, *J. Phys. Chem. Lett.*, 2017, **8**, 4557–4564.
15 S. Cheng and H. Zhong, *J. Phys. Chem. Lett.*, 2022, **13**, 2281–2290.
16 C. Caddeo, M. I. Saba, S. Meloni, A. Filippetti and A. Mattoni, *ACS Nano*, 2017, **11**, 9183–9190.
17 D. Ju, X. Zheng, J. Liu, Y. Chen, J. Zhang, B. Cao, H. Xiao, O. F. Mohammed, O. M. Bakr and X. Tao, *Angew. Chem., Int. Ed.*, 2018, **57**, 14868–14872.
18 L. Romani, A. Speltini, F. Ambrosio, E. Mosconi, A. Profumo, M. Marelli, S. Margadonna, A. Milella, F. Fracassi, A. Listorti, F. De Angelis and L. Malavasi, *Angew. Chem., Int. Ed.*, 2021, **60**, 3611–3618.
19 D. Ju, G. Lin, H. Xiao, Y. Zhang, S. Su and J. Liu, *Sol. RRL*, 2020, **4**, 2000559.

20 Yukta, M. K. Chini, R. Ranjan and S. Satapathi, *ACS Appl. Electron. Mater.*, 2021, **3**, 1572–1582.

21 S. Teale, M. Degani, B. Chen, E. H. Sargent and G. Grancini, *Nat. Energy*, 2024, **9**, 779–792.

22 T. Niu, J. Lu, X. Jia, Z. Xu, M.-C. Tang, D. Barrit, N. Yuan, J. Ding, X. Zhang, Y. Fan, T. Luo, Y. Zhang, D.-M. Smilgies, Z. Liu, A. Amassian, S. Jin, K. Zhao and S. Liu, *Nano Lett.*, 2019, **19**, 7181–7190.

23 L. Romani, A. Bala, V. Kumar, A. Speltini, A. Milella, F. Fracassi, A. Listorti, A. Profumo and L. Malavasi, *J. Mater. Chem. C*, 2020, **8**, 9189–9194.

24 Y. Gao, E. Shi, S. Deng, S. B. Shiring, J. M. Snaider, C. Liang, B. Yuan, R. Song, S. M. Janke, A. Liebman-Pelaez, P. Yoo, M. Zeller, B. W. Boudouris, P. Liao, C. Zhu, V. Blum, Y. Yu, B. M. Savoie, L. Huang and L. Dou, *Nat. Chem.*, 2019, **11**, 1151–1157.

25 J. V. Passarelli, D. J. Fairfield, N. A. Sather, M. P. Hendricks, H. Sai, C. L. Stern and S. I. Stupp, *J. Am. Chem. Soc.*, 2018, **140**, 7313–7323.

26 A. Merz and F. Ellinger, *Synthesis*, 1991, 462–464.

27 I. Spanopoulos, I. Hadar, W. Ke, P. Guo, S. Sidhik, M. Kepenekian, J. Even, A. D. Mohite, R. D. Schaller and M. G. Kanatzidis, *J. Am. Chem. Soc.*, 2020, **142**, 9028–9038.

28 A. Liang, K. Ma, Y. Gao and L. Dou, *Small Struct.*, 2022, **3**, 2100173.

29 K. Wang, L. Jin, Y. Gao, A. Liang, B. P. Finkenauer, W. Zhao, Z. Wei, C. Zhu, T.-F. Guo, L. Huang and L. Dou, *ACS Nano*, 2021, **15**, 6316–6325.

30 H. Hu, T. Salim, B. Chen and Y. M. Lam, *Sci. Rep.*, 2016, **6**, 33546.

31 M.-H. Tremblay, J. Bacsa, B. Zhao, F. Pulvirenti, S. Barlow and S. R. Marder, *Chem. Mater.*, 2019, **31**, 6145–6153.

32 C. C. Stoumpos, D. H. Cao, D. J. Clark, J. Young, J. M. Rondinelli, J. I. Jang, J. T. Hupp and M. G. Kanatzidis, *Chem. Mater.*, 2016, **28**, 2852–2867.

33 H. Zhao, K. Kordas and S. Ojala, *J. Mater. Chem. A*, 2023, **11**, 22656–22687.

34 J. Yang, T. He, M. Li, G. Li, H. Liu, J. Xu, M. Zhang, W. Zuo, R. Qin, M. H. Aldamasy, M. Yuan, Z. Li, M. M. Byranvand, M. Saliba and A. Abate, *ACS Energy Lett.*, 2022, **7**, 4451–4458.

35 M. Martynow, D. Glowienka, Y. Galagan and J. Guthmuller, *ACS Omega*, 2020, **5**, 26946–26953.

36 B. Chen, S. Wang, Y. Song, C. Li and F. Hao, *Chem. Eng. J.*, 2022, **430**, 132701.

37 Y. Li, X. Xu, C. Wang, B. Ecker, J. Yang, J. Huang and Y. Gao, *J. Phys. Chem. C*, 2017, **121**, 3904–3910.